Driven Drops on Heterogeneous Substrates: Onset of Sliding Motion

Uwe Thiele
Max-Planck-Institut für Physik komplexer Systeme, Nöthnitzer Strasse 38, D-01187 Dresden, Germany

Edgar Knobloch
Department of Physics, University of California, Berkeley, California 94720, USA

(Received 9 March 2006; published 15 November 2006)

Pinning and depinning of driven drops on heterogeneous substrates is studied as a function of the driving and heterogeneity amplitude. Two types of heterogeneity are considered: a "hydrophobic" defect that blocks the drop in front and a "hydrophilic" one that holds it at the back. Two different types of depinning leading to sliding motion are identified, and the resulting stick-slip motion is studied numerically.

DOI: 10.1103/PhysRevLett.97.204501 PACS numbers: 47.20.Ky, 47.55.D−, 68.08.−p, 68.15.+e

It is well known that liquid drops on an ideally smooth substrate move in response to external gradients. For example, a drop on an inclined substrate slides downslope in response to the gradient of potential energy [1,2]. Likewise, a drop in a temperature gradient moves towards lower temperatures as a result of Marangoni forces caused by surface tension gradients [3]. A wettability gradient induced by a chemical grading of the substrate also results in drop motion: The drop moves towards the most wettable region in order to minimize its energy [4,5].

Although on ideally smooth substrates drops will move even for arbitrarily small gradients, this is not the case for the "real" substrates used in experiments where the onset of drop motion is strongly influenced by spatial heterogeneities such as surface topography, wettability defects, or variations in the substrate temperature [6]. Variations in the electric field act in a similar way as wettability defects on drops in a condensor [7]. In all such systems, a finite driving force is necessary to overcome the pinning influence of the heterogeneities [8–15]. On the smaller, atomic scale, surface heterogeneities can trap drops even on very smooth surfaces. Indeed, heterogeneities occurring on a micro- or mesoscale are known to affect the macroscopic movement of drops and are responsible, for instance, for the observed hysteresis between advancing and receding contact angles, as well as for the observed roughening of contact lines [16–20].

The simplest example of depinning is described by the Adler equation [21]

$$\dot{\theta} = \mu - \sin\theta, \tag{1}$$

where θ represents the drop position, and $\mu > 0$ represents the applied force. When $\mu < 1$, a pair of fixed points is present, one of which is stable and the other unstable. At $\mu = 1$, these annihilate in a saddle-node bifurcation, producing periodic motion for $\mu > 1$. This result is simplest to understand if we write Eq. (1) as $\dot{\theta} = -dV/d\theta$, $V \equiv -\mu\theta - \cos\theta$. Evidently, Eq. (1) represents an overdamped particle in a cosinusoidal potential that is progressively tilted as μ increases. A "particle" in a stable equilibrium at a local minimum of this potential "spills out" once the tilt becomes large enough that its position no longer corresponds to a minimum. This occurs precisely at $\mu = 1$. The periodic motion present for $\mu > 1$ corresponds to the particle sliding down the resulting "washboard" potential. The period of this motion diverges as $(\mu - 1)^{-1/2}$ [22]. The resulting bifurcation is sometimes called a saddle-node infinite period bifurcation or "sniper" for short.

In this Letter, we explore the dynamics associated with the depinning of driven drops or ridges pinned by a heterogeneity. For simplicity, we choose a generic dynamical model describing drops on a solid substrate coexisting with a thin film [23–25] and model the effects of heterogeneity through a well-defined spatially periodic perturbation (Fig. 1). Random heterogeneities [18–20,26] are not considered. The system is driven by a lateral force $\tilde{\mu}$. In two dimensions, the model takes the form of an evolution equation for the film thickness profile $h(x, t)$ derived from the Navier-Stokes equation using the long-wave approximation [23]:

$$\partial_t h = -\partial_x\left(\frac{h^3}{3\eta}\{\partial_x[\gamma\partial_{xx}h + P(h, x)] + \tilde{\mu}\}\right). \tag{2}$$

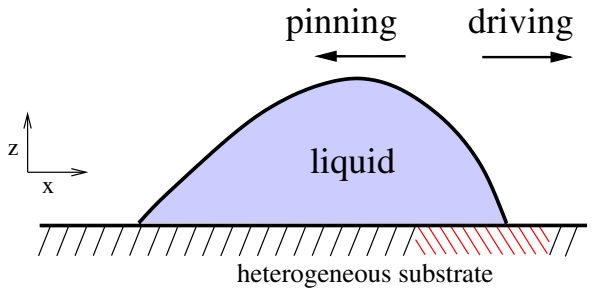

FIG. 1 (color online). Sketch of a drop on a heterogeneous substrate subject to a horizontal force towards the right.

Here γ is the surface tension, η is the dynamic viscosity, while $P(h, x)$ is an additional pressure term accounting for wettability, heating, electric field, etc. [27]. As an example, we use the disjoining pressure $P(h, x) = \tilde{\kappa}[b/h^3 - \tilde{\xi}(x) \times \exp(-h/l)]$ describing the wetting properties of the substrate [17,24,28,29]. This disjoining pressure corresponds to a combination of a long-range power law and a short-range exponential interaction [28,30], with the short-range component capturing the effects of spatial heterogeneity through the coefficient $\tilde{\xi}(x)$. The overall strength of the interaction with the substrate is measured by the energy density scale $\kappa = \tilde{\kappa}/l^3$. Any qualitatively similar pressure P yields like results, as shown for dewetting in Ref. [24], heated wetting films in Ref. [31], and for chemically driven running drops in Ref. [32]. When $\tilde{\mu} = 0$, the resulting model describes static drops with a finite mesoscopic equilibrium contact angle sitting on a precursor film.

In the following, we nondimensionalize Eq. (2) using the scales $3\eta\gamma/\kappa^2 l$ for time and $\sqrt{l\gamma/\kappa}$ for the lateral coordinate. The film thickness is scaled by the interaction length l that provides a characteristic scale for the thickness of the precursor film. In addition, we define the dimensionless volume force $\mu = (\gamma l/\kappa^3)^{1/2}\tilde{\mu}$. To identify the basic dynamical mechanisms responsible for depinning, we restrict our attention to drops not much thicker than the wetting layer. This case includes not only nanodrops on ultrathin precursor films ($l \approx 1, \ldots, 10$ nm) but also microdrops on macroscopic wetting layers ($l \approx 10, \ldots, 100$ μm). In the latter case, the pressure P may include the influence of temperature and/or electric fields [27,31,33], in addition to wettability in the form of repulsive van der Waals interactions. The spatial modulation responsible for pinning can then arise from any of the terms contributing to P. In the following, we call any heterogeneity that attracts [repels] liquid a hydrophilic [hydrophobic] defect.

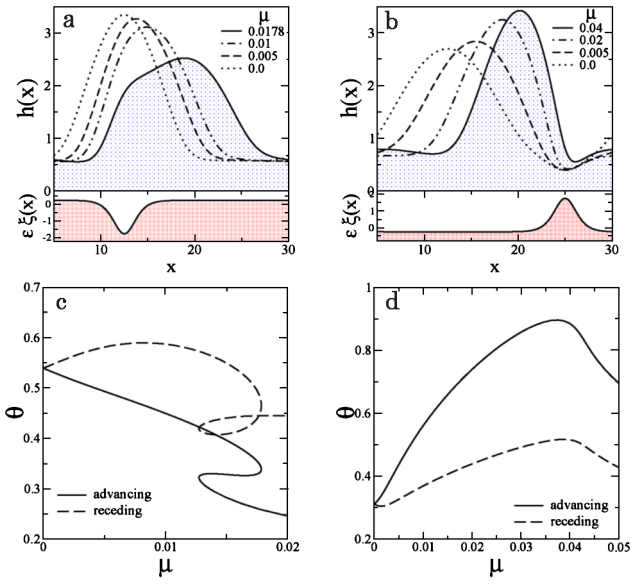

FIG. 2 (color online). Characteristics of pinned drops as a function of the forcing μ for localized hydrophilic [(a) and (c), $\epsilon = -1$] and hydrophobic [(b) and (d), $\epsilon = 1$] defects. The upper parts of (a) and (b) show steady drop profiles, while the lower parts show the wettability profile [Eq. (4) with $s = 6$]. The profile at depinning is shaded. In (a), the drop is pinned by a more wettable defect at the back, whereas in (b) it is blocked by a less wettable defect in front; (c) and (d) show the advancing and receding contact angles θ as a function of μ. The remaining parameters are $L = 25$, $b = 0.1$, and $\bar{h} = 1.5$.

Figures 2(a) and 2(b) show sample steady state profiles for two cases: (a) a hydrophilic defect and (b) a hydrophobic defect. Both are described by

$$P(h, x) = \frac{b}{h^3} - [1 + \epsilon\xi(x)]e^{-h}, \tag{3}$$

with a dimensionless coefficient b and

$$\xi(x) = \{2\mathrm{cn}(2K(k)x/L, k)\}^2 - \Delta, \tag{4}$$

where $K(k)$ is the complete elliptic integral of the first kind and Δ is such that the average of $\xi(x)$ over a spatial period L vanishes. We use the logarithmic measure $s \equiv -\log(1 - k)$ to quantify the steepness of the heterogeneity profiles [Figs. 2(a) and 2(b)]. In Fig. 2(a), the drop is held at the back by a hydrophilic defect ($\epsilon < 0$) and develops a prominent shoulder as μ increases just prior to depinning. In contrast, in Fig. 2(b), the hydrophobic defect ($\epsilon > 0$) blocks the drop and its profile steepens with increasing μ. The profiles at depinning are shaded. Figures 2(c) and 2(d) show the advancing and receding mesoscopic contact angles, measured at the inflection points of the drop profile, as a function of μ. For a drop pinned at the back [Fig. 2(c)],

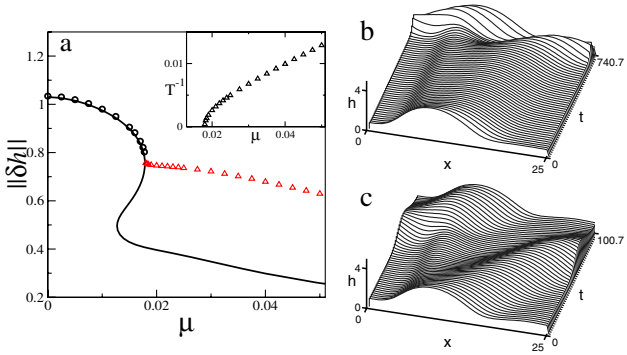

FIG. 3 (color online). (a) Bifurcation diagram for depinning via a sniper bifurcation for a hydrophilic defect [Eq. (4) with $s = 6$] with $\epsilon = -1.0$ and $L = 25$, $b = 0.1$, $\bar{h} = 1.5$. The figure shows the L^2 norm of steady solutions (solid line), selected steady solutions as obtained by integration in time (circles), and the time-averaged L^2 norm for the unsteady solutions beyond depinning (triangles). The inset shows the inverse of the temporal period T for the latter. The remaining panels show space-time plots over one spatial and temporal period for a sliding drop (b) close to depinning at $\mu = 0.0185$ with $T = 740.7$ and (c) far from depinning at $\mu = 0.04$ with $T = 100.7$.

the advancing [receding] angle decreases [increases] for small but increasing driving. However, once the drop starts developing a shoulder at the back, the receding angle decreases again until depinning occurs. The situation differs for a drop pinned at the front [Fig. 2(d)]. In this case, both angles increase with μ but drop just prior to depinning.

The depinning process corresponds to the loss of stability of the pinned drop. The stability calculation [34] reveals two mechanisms that lead to depinning. The first is via a sniper bifurcation (i.e., a steady state bifurcation) and prevails for hydrophobic defects with small wettability contrast [34] and for hydrophilic defects. Figure 3(a) shows a typical bifurcation diagram for the latter case as a function of increasing μ. The figure shows the L^2 norm of $\delta h \equiv h(x) - \bar{h}$, $\bar{h} \equiv L^{-1} \int_0^L h(x)dx$, for pinned drops and its time average after depinning. Although there are two saddle-node bifurcations in the diagram, time integration (open circles) shows that the upper part of the branch of pinned drops is stable until the rightmost saddle-node bifurcation. Thereafter, the solutions are time-dependent but periodic (open triangles). The inset shows that near the saddle-node the period diverges like $(\mu - \mu_c)^{-1/2}$ and, hence, that in this case depinning corresponds to a sniper bifurcation. Figures 3(b) and 3(c) show space-time plots of the resulting motion for (b) $\mu \gtrsim \mu_c$, and (c) $\mu = 0.04$. In Fig. 3(b), the drop spends a long time in a nearly stationary state while slowly spreading downstream, before it abruptly breaks off and moves towards the next defect. The resulting dynamics resembles a stretch-slip-stick motion. In contrast, in Fig. 3(c), the drop flows more or less at constant speed downstream, although the location of the defect remains visible in the space-time plot.

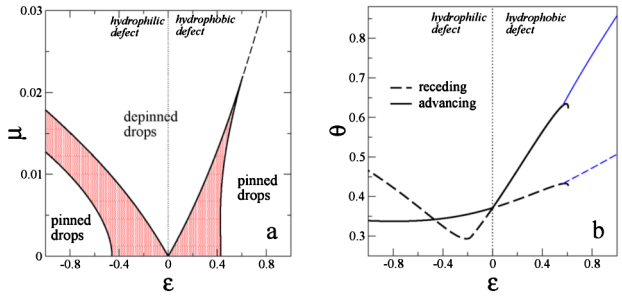

FIG. 4 (color online). (a) Phase diagram for the depinning transition for localized hydrophilic ($\epsilon < 0$) or hydrophobic ($\epsilon > 0$) defects [Eq. (4) with $s = 6$]. The figure focuses on a small wettability contrast for $L = 25$, $b = 0.1$, $\bar{h} = 1.5$. The solid (dashed) lines correspond to saddle-node (Hopf) bifurcations. The latter emerge near the cusp at which the two saddle-node bifurcations annihilate for $\epsilon > 0$. (b) Advancing (solid lines) and receding (dashed lines) contact angles θ at the depinning transition as a function of wettability contrast for a hydrophilic defect at the back ($\epsilon < 0$) and a hydrophobic defect at the front ($\epsilon > 0$). The thick (thin) lines refer to depinning through a real (oscillatory) mode.

Figure 4(a) shows the location of the two saddle nodes in the (ϵ, μ) plane. In the case of a hydrophilic defect ($\epsilon < 0$), the saddle nodes are always present; the one at larger μ corresponds to the depinning bifurcation. For fixed $\bar{h}$ and large L, the critical μ decreases as $1/L$ (not shown), as expected on the basis of simple loading ideas. However, Fig. 4 also shows that something else happens for sufficiently hydrophobic defects. Here the saddle nodes annihilate at $\epsilon \approx 0.6$, and depinning now occurs via a Hopf bifurcation (dashed line). The resulting bifurcation diagram [Fig. 5(a)] shows that the range of stable pinned profiles overlaps with the range of sliding drops generated by this instability. As μ decreases, the latter states lose stability at a saddle-node bifurcation, and the system settles into a time-independent pinned state in a hysteretic transition. Figures 5(b) and 5(c) show space-time plots of the sliding state both near this transition and further away. Here the depinning is as abrupt as for a hydrophilic defect [Fig. 3(b)] but without the associated stretching. However, farther away from the transition the depinned states in both cases look alike: In both cases, the drop travels at almost constant speed, only slightly modulated by the heterogeneity.

The advancing and receding angles at depinning (shaded profiles in Fig. 2) shown in Fig. 4(b) provide a measure of the contact angle hysteresis. In the case of a hydrophobic defect at the front ($\epsilon > 0$), both angles increase nearly linearly with defect strength and continue to do so even for oscillatory depinning ($\epsilon \gtrsim 0.6$); the small hook visible in the figure near this transition indicates that the Hopf bifurcation sets in prior to the disappearance of the saddle-node bifurcations. The behavior is more intricate when the pinning is by a hydrophilic defect at the back ($\epsilon < 0$). In this case, the role of the two angles is reversed, and both decrease nearly linearly with slopes identical to those in the $\epsilon > 0$ case. For $\epsilon < -0.2$, however, the receding angle reverses tendency and starts to increase again, while the

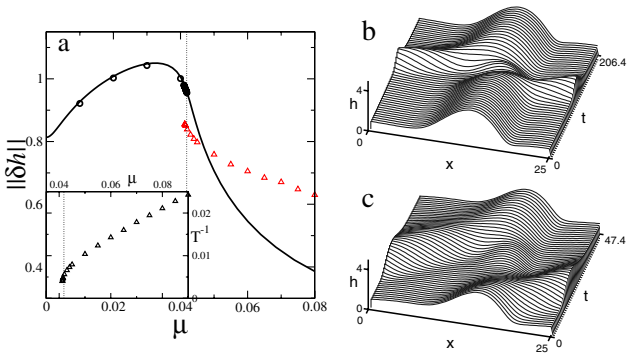

FIG. 5 (color online). As for Fig. 3 but showing depinning via a Hopf bifurcation when $\epsilon = 1.0$. (a) Bifurcation diagram. (b) Space-time plot for $\mu = 0.0415$ with $T = 206.4$. (c) $\mu = 0.08$ with $T = 47.4$. The vertical line indicates the location of the Hopf bifurcation as obtained from linear stability theory [34].

advancing angle continues to decrease. This change in behavior is a consequence of the stretching of the drop with increasing driving just prior to depinning: For $\epsilon \lesssim -0.2$, the force drags the main body of liquid downstream (to the right) but the spot of higher wettability traps part of it upstream. For fixed μ, the latter effect becomes more pronounced as $|\epsilon|$ increases; cf. Fig. 4(b).

We have examined the dynamics of depinning of drops on heteregeneous substrates subject to a driving force; besides gravity, possible driving forces include centrifugal forces and gradients of wettability, temperature, or electric fields. We have studied two types of pinning, by a hydrophilic defect at the back of the drop or by a hydrophobic defect in front, and identified two mechanisms whereby depinning takes place. In the case of a sufficiently large hydrophilic defect, the drop stretches markedly just prior to depinning as the driving increases; the drop loses stability at a saddle-node bifurcation, resulting in periodically modulated drop motion with an average speed that vanishes as $(\mu - \mu_c)^{1/2}$. We have referred to this type of bifurcation as a sniper. The resulting motion is slow when the drop is stretching and fast once the drop breaks away from a defect and spills onto the next one. The situation is richer for hydrophobic defects that pin the drop by blocking it. In this case, in addition to the steady state sniper bifurcation, a new depinning mechanism was observed with increased driving: The drop loses stability to an oscillatory mode prior to depinning. In the example shown, this bifurcation is hysteretic and the motion sets in with finite speed. Physically, the oscillations represent a rocking motion of the drop driven by the $O(\tilde{\mu} l^3)$ flow in the precursor film or wetting layer. Consequently, oscillatory depinning is possible only if the precursor flow is sufficiently large. This is not the case for nanodroplets driven by gravity; for such droplets, depinning always occurs via the sniper bifurcation. For large drops ($h_{\max} \gg l$), oscillatory depinning is also suppressed [34]. However, in dielectric liquids, a thick wetting layer of 100 nm to 1 μm stabilized by van der Waals interaction can coexist with microdroplets generated by an electric field [27,31,35], and both depinning mechanisms should be observable using gravity as the driving force.

This work was supported by NASA, NSF, and EU under Grants No. NNC04GA47G (E. K. and U. T.), No. DMS-0305968 (E. K.), and No. MRTN-CT-2004-005728 (U. T.).

[1] T. Podgorski, J.-M. Flesselles, and L. Limat, Phys. Rev. Lett. **87**, 036102 (2001).
[2] U. Thiele, M. G. Velarde, K. Neuffer, M. Bestehorn, and Y. Pomeau, Phys. Rev. E **64**, 061601 (2001).
[3] F. Brochard, Langmuir **5**, 432 (1989).
[4] E. Raphaël, C.R. Acad. Sci., Ser. II: Mec., Phys., Chim., Sci. Terre Univers. **306**, 751 (1988).
[5] M. K. Chaudhury and G. M. Whitesides, Science **256**, 1539 (1992).
[6] O. A. Kabov, Thermophys. Aeromech. **5**, 547 (1998).
[7] M. D. Morariu, N. E. Voicu, E. Schäffer, Z. Q. Lin, T. P. Russell, and U. Steiner, Nat. Mater. **2**, 48 (2003).
[8] L. W. Schwartz and S. Garoff, Langmuir **1**, 219 (1985).
[9] J. F. Joanny and M. O. Robbins, J. Chem. Phys. **92**, 3206 (1990).
[10] G. D. Nadkarni and S. Garoff, Langmuir **10**, 1618 (1994).
[11] A. Marmur, Colloids Surf. A **116**, 55 (1996).
[12] D. Quéré, M. J. Azzopardi, and L. Delattre, Langmuir **14**, 2213 (1998).
[13] E. Schäffer and P. Z. Wong, Phys. Rev. E **61**, 5257 (2000).
[14] P. Roura and J. Fort, Phys. Rev. E **64**, 011601 (2001).
[15] U. Thiele, L. Brusch, M. Bestehorn, and M. Bär, Eur. Phys. J. E **11**, 255 (2003).
[16] E. B. Dussan, Annu. Rev. Fluid Mech. **11**, 371 (1979).
[17] P.-G. de Gennes, Rev. Mod. Phys. **57**, 827 (1985).
[18] M. O. Robbins and J. F. Joanny, Europhys. Lett. **3**, 729 (1987).
[19] D. Ertas and M. Kardar, Phys. Rev. E **49**, R2532 (1994).
[20] R. Golestanian and E. Raphaël, Europhys. Lett. **55**, 228 (2001).
[21] R. Adler, Proc. IRE **34**, 351 (1946).
[22] S. H. Strogatz, *Nonlinear Dynamics and Chaos* (Addison-Wesley, Reading, MA, 1994).
[23] A. Oron, S. H. Davis, and S. G. Bankoff, Rev. Mod. Phys. **69**, 931 (1997).
[24] U. Thiele, K. Neuffer, Y. Pomeau, and M. G. Velarde, Colloids Surf. A **206**, 135 (2002).
[25] U. Thiele, Eur. Phys. J. E **12**, 409 (2003).
[26] P. Le Doussal, K. J. Wiese, E. Raphaël, and R. Golestanian, Phys. Rev. Lett. **96**, 015702 (2006).
[27] D. Merkt, A. Pototsky, M. Bestehorn, and U. Thiele, Phys. Fluids **17**, 064104 (2005).
[28] A. Sharma, Langmuir **9**, 861 (1993).
[29] J. N. Israelachvili, *Intermolecular and Surface Forces* (Academic, London, 1992).
[30] U. Thiele, M. G. Velarde, and K. Neuffer, Phys. Rev. Lett. **87**, 016104 (2001).
[31] M. Bestehorn, A. Pototsky, and U. Thiele, Eur. Phys. J. B **33**, 457 (2003).
[32] K. John, M. Bär, and U. Thiele, Eur. Phys. J. E **18**, 183 (2005).
[33] U. Thiele and E. Knobloch, Physica (Amsterdam) **190D**, 213 (2004).
[34] U. Thiele and E. Knobloch, New J. Phys. (to be published).
[35] Z. Q. Lin, T. Kerle, S. M. Baker, D. A. Hoagland, E. Schäffer, U. Steiner, and T. P. Russell, J. Chem. Phys. **114**, 2377 (2001).